

See discussions, stats, and author profiles for this publication at: <https://www.researchgate.net/publication/224989037>

# The spiral grid: A new approach to discretize the sphere and its application to mantle convection

**Article** in *Geochemistry, Geophysics, Geosystems* · February 2008

DOI: 10.1029/2007GC001581 · Source: DLR

---

CITATIONS

56

---

READS

3,530

2 authors, including:



**Christian Hüttig**

German Aerospace Center (DLR)

58 PUBLICATIONS 700 CITATIONS

SEE PROFILE

# **The Spiral Grid: A New Approach to Discretize the Sphere and Its Application to Mantle Convection**

**CHRISTIAN HÜTTIG - KAI STEMMER**

Institute of Planetary Research, German Aerospace Center (DLR), Berlin, Germany

This paper presents a new method to generate a three-dimensional spherical grid using natural neighbor Voronoi cells distributed by spiral functions. A unique property of this grid is the complete removal of symmetries with arbitrary selectable lateral and radial resolution, which are not restricted to discrete radial levels or geometrical constraints as compared to the commonly used grids based on projected triangulated platonic solids such as a cube, rhomboid or an icosahedron. The spiral grid can be refined in certain areas of interest and makes it possible to have a very small inner radius to outer radius ratio. Cell volumes can be made almost constant throughout the computational domain. Analysis, statistics and computation methods are described in detail, as well as a possible domain decomposition suitable for parallel computing. Conductive temperature profiles were numerically calculated in the spherical shell and directly compared with the analytic solution as verification. The grid is applied to numerical simulations of mantle convection using a finite volume scheme. The model is validated by a comparison of steady-state cubic and tetrahedral convection patterns with other published models.

## **1. Introduction**

In the last twenty years numerical simulation codes of thermal convection have proved to be powerful tools for getting a closer look into the dynamics of the Earth and other planets. The massive increase in computational power especially in recent years allows for the simulation of mantle convection in fully three-dimensional spherical shells. For such geodynamic simulations, spherical grids are a necessary base for the numerical model. The widely used latitude-longitude grid in combination with a spectral approach is well suited for spherical convection provided there are only constant or radially variable fluid properties [Glatzmaier, 1988; Tackley et al., 1993; Harder, 1998]. However, this approach is tedious for lateral variable fluid properties like a temperature-, pressure- and stress-dependent rheology, which is assumed for the Earth's mantle from theoretical and experi-

mental studies [Weertmann, 1970; Karato and Wu, 1993]. With local methods like finite differences, finite volumes or finite elements to discretize the differential equations, two crucial difficulties occur when spherical coordinates are used. The singularities at the poles and the grid convergence towards the poles limit the applicability of local methods to a latitude-longitude grid. While the singularity problem at the poles is solvable [Kageyama et al., 1995], the problem of the grid convergence is more serious and introduces a restriction to the time-step length [Ratcliff et al, 1996; Iwase, 1996].

Since no grid is orthogonal all over the spherical surface and at the same time free of coordinate singularities and grid convergence, the spherical surface is usually split up into sub-regions. To distribute points uniformly on a sphere, most grids are based on triangulated platonic solids, which radially project from the center. Complex grids based on subdivisions of platonic solids like the icosahedron grid [Baumgardner, 1985], the rhomboid grid [Zhong et al., 2000], the Yin-Yang grid [Yoshida and Kageyama, 2004], the cubed-sphere grid [Choblet, 2005; Ronchi 1996] and the smoothed cubed-sphere grid [Stemmer et al., 2006] prevail for modeling mantle convection in a spherical shell. These grids have axisymmetric alignments that simplify the discretization schemes in the form of algebraic descriptions and make possible the use of multigrid methods, but also cause some restrictions. Firstly the user can only choose between fixed resolution step sizes that increase the total number of grid points in preset steps. For example, increasing the resolution by the next possible step in an icosahedral refinement results in about eight times more grid points [Baumgardner, 1985]. Secondly the volume and neighbor distance of a cell depends on its radius, i.e. on the inner surface of the spherical shell the grid points are arranged more densely than on the outer surface.

The spiral grid can avoid these disadvantages using an almost uniform distribution of grid points from the Archimedean spiral equation, which is modified to create a spherical shell. These Cartesian functions lead to extremely dense points at the poles in comparison to the equator of the sphere when advancing them over an angular variable. Obtaining an equidistant distribution over a constant arc length requires the inversion of elliptic integrals. Distributing the spherical spiral over increasing radii result in a shell-based point cloud with an average distance between neighbors of a desired resolution.

## 2. Discretization of the Spherical Shell

Layers of spirals with a constantly or variably increasing radius form a three-dimensional spherical shell from a desired inner to outer radius. These spirals are discretized to point shells, which act as generator points for the Voronoi diagram (VD). An equidistant discretization along the Archimedean spiral guarantees a nearly uniform distribution. The VD provides cells as arbitrary convex polyhedral that through its unique properties suit a finite-volume method (FVM).

### 2.1. Archimedean Spiral Equation

The basic equation for the two-dimensional Archimedean spiral in polar coordinates is given by

$$(1) \quad r = f(\varphi) = a \cdot \varphi$$

where  $r$  is the radius and  $a$  the increment multiplier of the angle  $\varphi$ . For a two-dimensional Cartesian representation, the two parametric equations for each coordinate evolving over an angular variable,  $a$ , are given by

$$(2) \quad \begin{aligned} x &= f(a) = a \cdot \sin(a) \\ y &= f(a) = a \cdot \cos(a) \end{aligned}$$

Finally, the spiral mapped over a sphere in three-dimensional Cartesian coordinates, evolving from zero to  $a_{\max}$ , which is from the north pole to the south pole, is provided by

$$(3) \quad \begin{aligned} x &= f(a) = r \cdot \cos(a) \cdot \cos\left(\frac{-\pi}{2} + \frac{a}{a_{\max}} \cdot \pi\right) \\ y &= f(a) = r \cdot \sin(a) \cdot \cos\left(\frac{-\pi}{2} + \frac{a}{a_{\max}} \cdot \pi\right) \\ z &= f(a) = r \cdot \sin\left(\frac{-\pi}{2} + \frac{a}{a_{\max}} \cdot \pi\right) \end{aligned}$$

where  $2 a_{\max} / \pi$  determines the amount of complete revolutions of the spiral on the sphere with a radius of  $r$ .

The intention behind this discretization method is to distribute points along the spiral path with a constant user-chosen distance, which results in a uniform cell resolution on the spherical shell. The equation for the arc length from (1) and (2) is

$$(4) \quad s = \frac{1}{2} a \left( \varphi \sqrt{1 + \varphi^2} + \log \left[ \varphi \sqrt{1 + \varphi^2} \right] \right),$$

which cannot be solved for  $\varphi$  analytically. The general equation for the arc length in three-dimensional Cartesian coordinates is given as

$$(5) \quad s = \int \sqrt{\partial_x a^2 + \partial_y a^2 + \partial_z a^2} da.$$

The following equation evolves by using (3) with (5):

$$(6) \quad s = r E \left[ \frac{\pi a}{a_{\max}}, -\frac{a_{\max}^2}{\pi^2} \right]$$

This equation includes the second incomplete elliptic integral  $E[a, m]$ , which is defined as

$$(7) \quad E[a, m] = \int_0^a \sqrt{1 - m \cdot \sin^2(\theta)} d\theta,$$

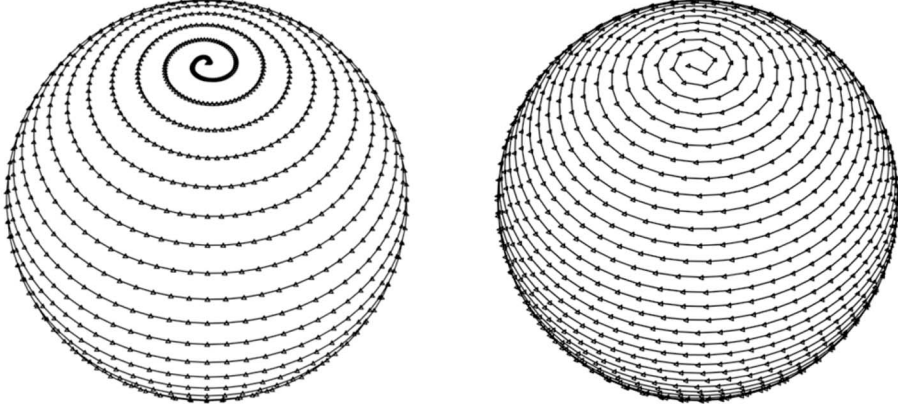


FIGURE 1. – *The spherical spiral with a constant angular increase (left) and its equidistant version (right) from a preset point distance.*

where  $m$  is the elliptic modulus. By increasing  $a$  with a constant value, the points become very dense around the poles and sparse on the equator, as illustrated in figure 1a. To have a constant predefined distance along the spiral path, an inversion of the arc distance equation (6) for  $a$  is necessary. This inversion computes the location of the points for an equidistant distribution.

By applying equation (6) to find the angular values of  $a$  for the original three-dimensional Cartesian equation (3) of the spiral, an equidistant distribution of points along the spiral path appears on the sphere as shown in figure 1b. A numerical method proposed by Carlson and Notis (1981) reduces the computational costs to inverse the second incomplete elliptic integral used in (6).

Since  $a_{max}$  determines the revolutions of the spiral from the top to the bottom, it must be chosen properly to guarantee an equidistant distribution that fits the requested resolution. With a defined resolution  $R$  and layer radius  $r_i$ ,  $a_{max}$  is given by

$$(8) \quad a_{max} = \left( \frac{3\pi^2 r_i}{2R} \right).$$

## 2.2. Radial Extension of the Spiral Sphere

To create the generator points necessary for triangulation or Voronoi tessellation, the method described in 2.1 is repeated for several radii between a user-chosen inner and outer radius. This results in the layering of concentric spiral spheres. The equation to return the number of layers required for a certain global resolution is:

$$(9) \quad i_{max} = \frac{3(r_{outer} - r_{inner})}{4R} + 2$$

The number of generator points that result between two given radii and a

resolution  $R$  is given by

$$(10) \quad n_{\text{Points}} = \sum_{i=0}^{i_{\max}} \frac{1}{R} E \left[ \pi, \frac{6 \pi r_{\text{inner}}}{4R} + 2 \pi i \right].$$

The spherical shell consists of two additional boundary shells within the inner and outside the outer radius. To produce smooth inner and outer walls these points are exactly above (below) the last outer (inner) shell points. Those two boundary layers produce open polyhedra on the outside and core-connecting polyhedra on the inside. The boundary walls can be turned into spherical triangles for increased precision on low-resolution grids to improve accuracy and therefore will remain as the only cells with partial curved elements.

By “overtuning” the spiral equations on every second layer, where  $a$  evolves from  $a_{\max}$  to  $2a_{\max}$ , the standard deviation of the neighbor point distances can be reduced. The spiral would evolve from the south-pole to the north-pole in the opposite revolution. Starting  $a$  in equation (3) at  $R/2$  instead of zero leads to a reduction of the cell volume fluctuations at the poles as well (see statistics section 3, closeup of figure 4).

### 2.3. Cell Generation

The point distribution from these equations now allows a triangulation and Voronoi tessellation. This paper focuses on the Voronoi tessellation to generate polyhedral cells. After applying fast Voronoi algorithms from libraries like Barber et al., 1998, cells as in figure 2 emerge with typical Voronoi properties such as:

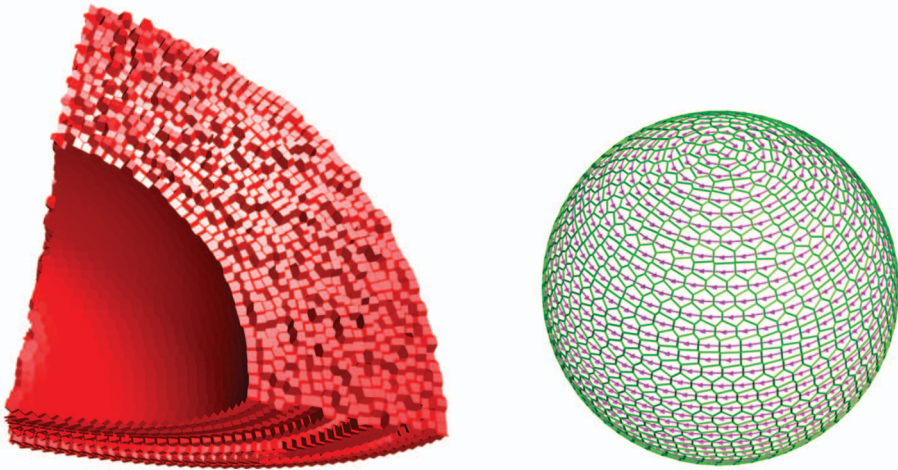


FIGURE 2. – Left: a cut through the positive Cartesian domain of the spiral grid with an inner radius of one, an outer radius of two and a resolution of 0.1, excluding the boundary shells; the complete grid consists of 62,529 cells. Right: a spherical Voronoi Diagram for one shell of spiral generator points.

- every wall distinguishes two generator points as natural neighbors
- every wall lies perpendicular to a line between two natural neighbors
- every wall is placed exactly between two natural neighbors
- every cell is convex

The process to calculate the spiral generator points takes approx. 0.05% of the time to compute the whole grid; the major time takes the Voronoi tessellation.

#### 2.4. Cell Center, Surface and Volume Calculation

To obtain some important properties such as the center of mass, volume and the surface of the cell walls, which appear in the discretization of differential equations and definition of the operators, some care was taken to optimize the surface and volume integrals to receive accurate and quick results.

The tetrahedron is the simplest object that can occupy space in three dimensions. Any simplex with  $n + 1$  coordinates within  $n$  dimensions is capable of this. The special properties of these simplexes remain within arbitrary dimensions: their center of mass is situated within the arithmetic mean of all coordinates and their  $n$ -dimensional volume can be computed by

$$(11) \quad V = \frac{1}{n!} \begin{vmatrix} x_{1,1} & \cdots & x_{1,n} & 1 \\ \vdots & \ddots & \vdots & \vdots \\ x_{n+1,1} & \cdots & x_{n+1,n} & 1 \end{vmatrix}.$$

The  $n + 1$  coordinates for an  $n$ -dimensional tetrahedron lie in the vertical direction of the matrix of equation (11). The algorithm to compute the centroid of a convex polyhedron uses these properties. It consists of the following steps:

- computing the arithmetic mean of all vertices, which results in a point guaranteed to be within the polyhedron
- projecting rays from this preliminary center to the faces of the polyhedron, resulting in possible deconstruction into tetrahedra
- computing the center of mass (COM) and volume of each tetrahedron
- weighting all COM by their volume to obtain the true COM of the polyhedron
- add all tetrahedral volumes to obtain the polyhedron volume

The areas of the cell walls were computed using a method described by [Sunday, 2002], with an advancement over the textbook equation for the area of an  $n$ -vertex two-dimensional polygon, which normally uses  $2n + 1$  multiplications and  $2n - 1$  additions. [Sunday, 2002] improves the equation so that it takes  $n + 1$  multiplications and  $2n - 1$  additions. A similar equation is derived for a three-dimensional planar polygon where, given the unit normal, the textbook equation cost of  $6n + 4$  multiplications and  $4n + 1$  additions is reduced to  $n + 2$  multiplications and  $2n - 1$  additions.

### 2.5. Centroidal Shift

A centroidal Voronoi diagram (CVD) is a specific Voronoi diagram (VD), where the associated generator points coincide with their centroids. The centroid is the center of mass of the corresponding Voronoi cell. Such tessellations are useful in data compression, optimal quadrature rules, optimal representation and quantization, finite difference schemes, optimal distribution of resources, cellular biology and the territorial behavior of animals, among other contexts (Alliez et al. 2005). Ju et al., 2001 describes in detail some of these applications and algorithms.

A common way to define finite difference schemes on irregular meshes for the approximate solution of partial differential equations is based on Voronoi tessellations and its dual grid, the Delaunay triangulation. In many cases, using centroidal Voronoi tessellations guarantee a second-order truncation error for the different equations compared to a first-order truncation error for other Voronoi tessellations. Similar results are known for co-volume methods based on the dual Voronoi-Delaunay tessellations. Lloyd's method provides one of two basic algorithms to iterate towards a CVD [MacQueen, 1967; Lloyd, 1982]. For an initial set of  $n$  points the procedure is as follows:

1. Determine the VD corresponding to the  $n$  generator points.
2. Determine the centroids with respect to a given density function of the  $n$  Voronoi cells.
3. Set the  $n$  generator points to their corresponding  $n$  centroids.
4. Repeat steps one to three until satisfactory convergence is achieved.

This method involves finding the centroids of the polyhedron. The centroid becomes the point where the partial differential equations are calculated. Note that the generator point from the spiral is not necessarily the centroid of the Voronoi-cell. The spiral spherical shell shows an advantage over other distribution methods because the centroid is already close to the generator point, which results in lesser iterations with the Lloyd method.

### 2.6. Domain Decomposition

To run a simulation with a reasonable resolution, the code must work with more than one CPU in parallel. Typically, a domain decomposition of the grid is applied, which results in an optimal breakdown of the grid into  $p$  equal volumes and therefore amount of domains and processors. An efficient domain decomposition minimizes the area between these sections, leading to a minimized overhead of data exchange between the processors.

Halo-cells, sometimes called ghost-cells, arise in domain decomposition as additional cells in each domain, which form an overlapping zone where data is exchanged. These cells border each domain and are on the same position as their active cells on the neighboring domain. The ratio between halo-cells and grid cells is a first measure of efficiency for parallelization. This ratio is vital to determine the amount of data transported between the domains.





FIGURE 3. – *The resulting halo-cells after a domain decomposition of the spiral grid with a resolution of 0.55 and 24 shells. Left: Domain decomposition for six CPUs (equal to the cube); Right: 32 CPUs.*

One approach to decomposing a sphere laterally is to distribute  $p$  points on the surface to minimize the global potential energy. This approach is known as the Thomson Problem [Thomson, 1904]. After this step, its closest “Thomson” point derives the domain affiliation for every cell. The resulting decomposition as shown in figure 3 leads to equal domain volumes, which is important to balance the computational efforts for each CPU. Some  $p$  reproduce platonic solids;  $p=4$  creates a tetrahedron,  $p=6$  a cube and  $p=12$  a dodecahedron. However, all  $p > 1$  show a certain symmetry [Wales and Ulker 2006].

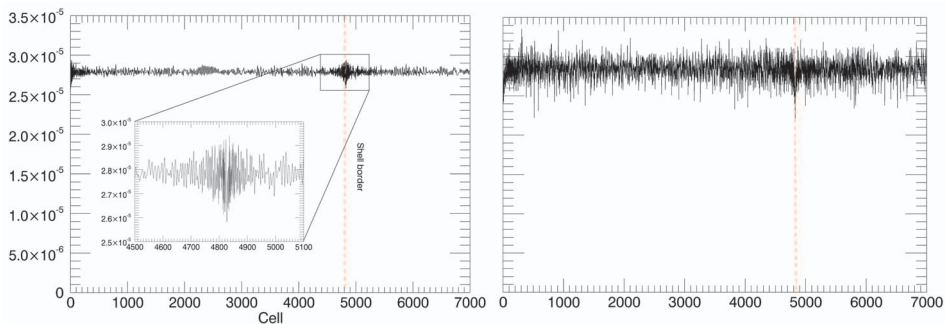


FIGURE 4. – *Cell volumes along the spiral path from the original VD distribution (left) and from the CVD shifted distribution (right). The straight line marks the transition to the next shell at the pole.*

### 3. Statistical Analysis

Statistical analyses of the original spiral grid and shifted spiral grid with the centroidal Voronoi diagram (CVD) are applied to highlight the advantages of this grid

structure. An inner radius of one and outer radius of two were taken to analyze the grid at a resolution of 0.1. Note that the stop criterion for the Lloyd iterations is a mean distance from the generator points to the true centroid of  $5 \cdot 10^{-6}$ , which results in approximately twelve iterations (as explained in section 2.5).

The centroidal shift demonstrates several advantages and disadvantages in the

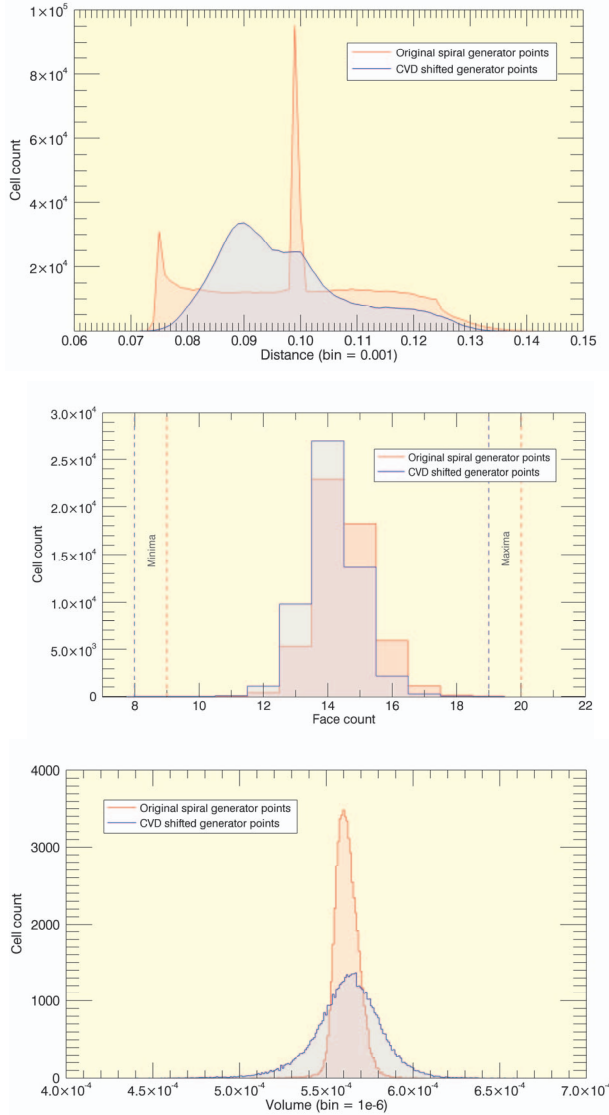


FIGURE 5. – Statistical analysis of the original spiral grid (VD, red) and the centroidal Voronoi diagram (CVD, blue) generated by shifting of the original grid points. a) PDF of the natural-neighbor distances. b) PDF of the number of faces per cell. c) PDF of the cell volume.

spiral spherical shell. The shift reduces the amount of Voronoi vertices and faces by about three percent, and yields a better standard deviation of the neighbor distances proven by figure 5 and table 1. Figure 4 illustrates the volume fluctuations within the cells along the spiral path before and after the centroidal shift and shows the effect of the increased standard deviation of the volumes after the shift. The peaks from the original distribution at the poles vanish.

TABLE 1. – Statistical values of the spiral grid with an inner radius of one, an outer radius of two and a resolution of 0.1 according to the PDFs of Figure 5. The complete grid consists of 62,529 cells. Distance describes the Euclidian distance between neighbors, Neighbor refers to the amount of neighbors per cell and volume specifies the cell volume.

|              | Gridtype | Minima    | Mean      | Maxima     | $\sigma$  | Skew   |
|--------------|----------|-----------|-----------|------------|-----------|--------|
| Distance PDF | VD       | 0.0733    | 0.0999    | 0.1435     | 0.01476   | 0.104  |
| Distance PDF | CVD      | 0.0716    | 0.0977    | 0.1383     | 0.01148   | 0.779  |
| Neighbor PDF | VD       | 10        | 14.513    | 20         | 0.93145   | 0.381  |
| Neighbor PDF | CVD      | 9         | 14.126    | 19         | 0.85666   | 0.156  |
| Volume PDF   | VD       | 5.0747e-4 | 5.6241e-4 | 6.14050e-4 | 6.7013e-6 | 0.111  |
| Volume PDF   | CVD      | 4.4102e-4 | 5.6271e-4 | 6.58129e-4 | 1.8974e-5 | -0.436 |

In figure 5a probability density functions (PDF) are plotted for the distances of adjacent cells, cell volumes and number of cell faces for the VD and CVD. With respect to the distance histogram, the peak in the original distribution is caused by the exact calculated distance along the spiral path. At least two neighbors of every cell have the pre-set resolution as distance to each other since there is one predecessor and one successor on the spiral path. This applies for all cells except the first and the last in one spiral. Note that the peak is slightly off the desired resolution since it is calculated along a curved spiral path, which results in a slightly smaller spatial distance. The CVD version shows a reduced standard deviation but a slight left shift and higher skew. The projected first and last boundary shell causes an irregularity in the distribution and first appears as the mentioned shift during the Lloyd iterations. These shells are projected to create a smooth boundary. Purely projected grids would have a much less pronounced peak because the distances of adjacent cells generally increase with increasing radius.

The face count PDF presented in figure 5b displays a major advantage of a CVD. The centroidal shift yields a reduction of Voronoi-faces and therefore vertices. The face count is equal to the amount of neighbors per cell and therefore matrix entries, so it reduces necessary calculations within the numerical discretization as well as resources and housekeeping information.

The peak for the volume histogram in figure 5c is less pronounced for the CVD compared to the VD, but the absolute volume differences are relatively small because the CVD grid is shifted to get centroidal characteristics. This is the only disadvantage of a CVD; the centroidal shift does not tend to equalize cells to their volume. Generator points can be positioned so that the resulting VD would be a CVD but with cells of different volume.

## 4. Application and Validation Tests of the Spiral Grid

To confirm the applicability of the spiral grid and the domain decomposition for fluid dynamic simulations, two test cases have been studied. A simple heat diffusion scenario in the spherical shell with fixed boundary conditions at the inner and outer radius is set up, which enables a comparison of the numerical solution based on the spiral grid with the analytical solution of the boundary value problem of the Poisson-equation. Furthermore, the spiral grid is applied to mantle convection simulations of steady-state convection patterns with a tetrahedral and cubic symmetry. While no analytical solution of this problem is known, the model is validated by a comparison of diagnostic parameters with other published models.

To examine the parallel performance of the domain decomposition from section 2.6, a suitable test scenario was chosen and executed on several different supercomputers and smaller shared memory machines. These results are illustrated in figure 6.

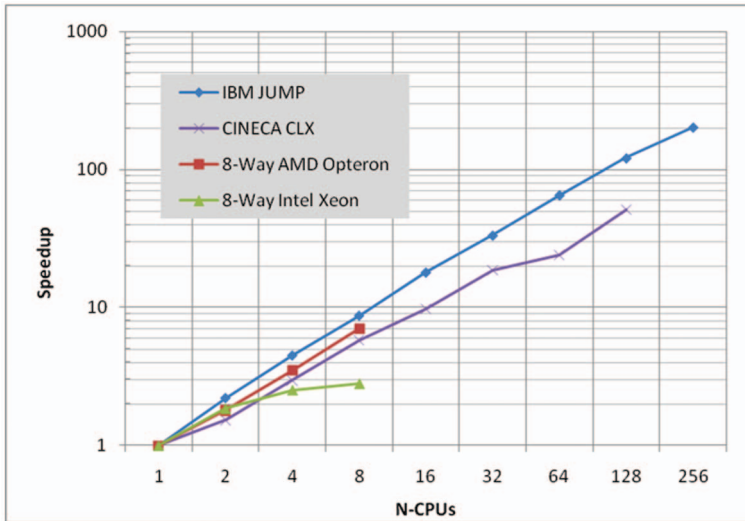


FIGURE 6. – Speedup graph for various CPU counts on the CLX supercomputer at CINECA (XEON cluster), the IBM JUMP (p690 cluster) at FZ-Juelich and two local shared memory systems with AMD 875 and INTEL XEON 5355 CPUs.

### 4.1. Heat Diffusion

The following Laplace equation illustrates the practicability of the spiral discretization through a comparison to analytic results, whereas  $\psi$  represents a scalar value within a discretized spherical shell.

$$(12) \quad \nabla^2 \psi = 0$$

The boundary conditions for this problem were preset Dirichlet on both layers, with a value of one at the inner radius and a value of zero at the outer radius. This is similar to a time-independent solution of heat transfer through the spherical shell, heated from below without internal heat sources or sinks. A finite volume discretization utilizing Gauss' theorem was applied to yield a solution for equation (12) on three different grid resolutions. Equation (13) represents the analytical solution to (12) for any discrete  $\psi_i$  within a spherical shell. The variables  $\psi_{outer}$  and  $\psi_{inner}$  represent the boundary condition for  $\psi$ ,  $r_{outer}$  and  $r_{inner}$  the outer / inner radius of the spherical shell,  $r_i$  the radius of  $\psi_i$ .

$$(13) \quad \psi_i = \psi_{inner} + \frac{r_{outer}(r_i - r_{inner})(\psi_{outer} - \psi_{inner})}{r_i(r_{outer} - r_{inner})}$$

In respect to heat diffusion, equation (12) and (13) produce a conductive temperature profile in a spherical shell.

To solve equation (12) on various grids, an implicit method using the freely available PETSc solver [Balay et al., 2004] was used on a single 64 bit Opteron with 2.2 GHz. The solver uses a block-Jacobian pre-conditioner with a Krylov-subspace CGstab method. Table 2 summarizes results for three grid resolutions for the Voronoi diagram (VD) and the centroidal Voronoi Diagram (CVD).

TABLE 2. – Comparison of the numerical and analytical solution of a boundary value problem describing a conductive temperature profile. Resolution denotes the grid spacing of the spiral grid with the respective number of nodes of the Voronoi diagram (VD) and the centroidal Voronoi Diagram (CVD). The mean absolute deviation, the standard deviation  $\sigma$ , the max absolute error are given each with the required computing time in seconds and the number of iterations, where S stands for the analytical and s for the numerical solution.

| Resolution | Nodes  | Gridtype | $ \overline{S} - s $ | $\sigma$ | $\ \overline{S} - s\ $ | CPU time<br>in seconds | Iterations |
|------------|--------|----------|----------------------|----------|------------------------|------------------------|------------|
| 0.04       | 106677 | VD       | 1.072E-3             | 1.513E-3 | 1.0745E-2              | 3.9                    | 25         |
| 0.03       | 266725 | VD       | 7.995E-4             | 1.112E-3 | 8.7012E-3              | 13.5                   | 34         |
| 0.02       | 815302 | VD       | 6.270E-4             | 8.539E-4 | 6.2967E-3              | 57.3                   | 47         |
| 0.04       | 106677 | CVD      | 7.502E-4             | 1.042E-3 | 1.0284E-2              | 3.8                    | 25         |
| 0.03       | 266725 | CVD      | 5.296E-4             | 7.356E-4 | 7.3207E-3              | 13.1                   | 33         |
| 0.02       | 815302 | CVD      | 4.412E-4             | 6.019E-4 | 5.9523E-3              | 57.0                   | 45         |

#### 4.2. Steady-State Mantle Convection

Mantle convection is considered as thermal convection of a Boussinesq fluid at infinite Prandtl-number heated from the bottom of the spherical shell. The ratio of the inner to the outer radius is 0.55 similar to the Earth's mantle. Boundary conditions are given by impermeable and free-slip conditions for the velocities with a fixed temperature  $T = 1$  at the inner and  $T = 0$  at the outer radius. The non-dimensional form of the equations of mass, energy and momentum conservation result from scaling the equations with intrinsic parameters like the thickness of the spherical shell  $d = 1$ , the

thermal diffusion time and the temperature difference  $\Delta T = 1$  between the boundaries.

$$\begin{aligned}
 (14) \quad & \nabla \cdot \mathbf{u} = 0 \\
 & \nabla^2 \mathbf{u} + Ra T \mathbf{e}_r \nabla p = 0 \\
 & \frac{\partial T}{\partial t} + \mathbf{u} \nabla T - \nabla^2 T = 0
 \end{aligned}$$

In this set of equations,  $T$  denotes the temperature,  $\mathbf{u}$  the flow velocity,  $p$  the dynamic pressure,  $t$  the time,  $\mathbf{e}_r$  the unit vector in radial direction and  $Ra$  the system parameter Rayleigh-number, which defines the ratio of buoyancy forces to resisting forces,

$$(15) \quad Ra = \frac{\rho g a \Delta T d^3}{\kappa \eta}$$

where  $\rho$  is the density,  $g$  the acceleration of gravity,  $a$  the coefficient of thermal expansion,  $\kappa$  the thermal diffusivity,  $\Delta T$  the temperature difference between bottom and top,  $d$  the thickness of the spherical shell and  $\eta$  the dynamic viscosity.

To solve equation (14), a finite volume discretization method with second-order accuracy with a co-located velocity / pressure alignment was used [Ferziger and Pécic, 2002]. In order to ensure mass conservation, the SIMPLE pressure correction algorithm [Patankar, 1980; Fletcher, 1991] is applied and combined with a pressure weighted interpolation method (PWI) [Rhie and Chow, 1983; Stemmer et al., 2006] to satisfy the incompressible condition and to avoid oscillatory pressure solution due to pressure decoupling. The Crank-Nicolson method ensures second order accuracy within time discretization. An implicit iterative solver, a block-jacobian pre-conditioner with a Krylov-subspace CGstab method [Balay et al., 2004], is implemented for solving the pressure correction equation in the SIMPLE algorithm as well as for the energy and momentum equation.

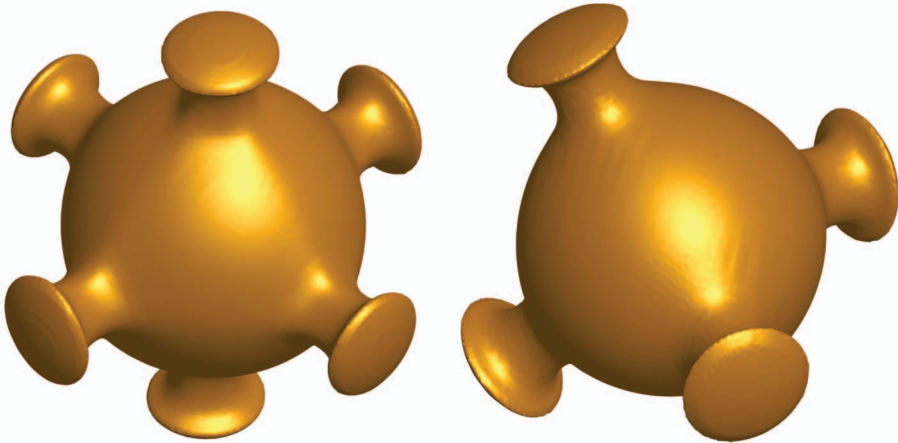


FIGURE 7. – The iso-surface of temperature with  $T = 0.5$  of a cubical (left) and tetrahedral (right) steady-state. The Rayleigh number is 7000 and the inner to outer radius ratio is 0.55.

Thermal convection in the spherical shell at infinite Prandtl-number has two stable solutions with polyhedral symmetry when the Rayleigh number is low [Busse, 1975; Schubert, 2001]. These steady-state flow patterns with tetrahedral and cubic symmetry are used to compare different published spherical models with various discretization schemes and numerical methods [Stemmer et al., 2006]. The tetrahedral symmetry has four upwellings and the cubic symmetry has six upwellings as displayed in figure 7.

To assure a steady-state solution, the diagnostic values (Nusselt number, root-mean-square velocity) should change less than  $10^{-6}$  in one time-step. Table 3 illustrates the resulting diagnostic parameters of steady-state convection in a spherical shell with a Rayleigh-number of  $Ra = 7000$  in comparison to other published models. The results agree well within a few percent. The remaining differences are due to different numerical grids, grid resolutions and discretization methods.

TABLE 3. – Comparison of bottom and top Nusselt numbers,  $Nu_{T0}$  and  $Nu_{T1}$ , and volume-averaged rms-velocities,  $v_{rms}$ , of tetrahedral and cubic steady-state flow patterns of thermal convection in a spherical shell. ‘Be89’ indicates results by Bercovici et al. (1989), ‘Zh00’ by Zhong et al. (2000), ‘Iw96’ by Iwase (1996), ‘TS00’ by Tabata and Suzuki (2000), ‘Ha98’ by Harder (1998), ‘Ra96’ by Ratcliff et al. (1996), ‘YK04’ by Yoshida and Kageyama (2004) and ‘St06’ by Stemmer et al. (2006). The respective discretization method is given where ‘SP’ indicates spectral, ‘FE’ finite elements, ‘FD’ finite differences and ‘FV’ finite volumes. Nodes denote the total number of nodes.

| Model | Method | Nodes   | tetrahedral (l, m) = (3, 2) |           |           | cubic (l, m) = (4, 0) + (4, 4) |           |           |
|-------|--------|---------|-----------------------------|-----------|-----------|--------------------------------|-----------|-----------|
|       |        |         | $Nu_{T0}$                   | $Nu_{T1}$ | $v_{rms}$ | $Nu_{T0}$                      | $Nu_{T1}$ | $v_{rms}$ |
| Be89  | SP     | 2400    | 3.4657                      | 3.5293    | —         | —                              | —         | —         |
| Zh00  | FE     | 165888  | 3.519                       | 3.427     | —         | —                              | —         | —         |
| Iw96  | FV     | 532480  | 3.45                        | —         | 32.4173   | —                              | —         | —         |
| TS00  | FE     | 324532  | 3.6565                      | —         | 32.936    | —                              | —         | —         |
| Ha98  | SP     | 552960  | 3.4955                      | —         | 32.6375   | 3.6086                         | —         | 31.0765   |
| Ra96  | FV     | 200000  | 3.4423                      | —         | 32.19     | 3.5806                         | —         | 30.87     |
| YK04  | FD     | 2122416 | 3.4430                      | —         | 32.0481   | 3.5554                         | —         | 30.5179   |
| St06  | FV     | 663552  | 3.4864                      | 3.4864    | 32.5894   | 3.5982                         | 3.5984    | 31.0226   |
| This  | FV     | 133084  | 3.5142                      | 3.5184    | 32.783    | 3.6137                         | 3.618     | 31.1679   |

## 5. Summary

We have developed a new spherical grid using natural neighbor Voronoi cells around points distributed by spiral functions, which is suitable for numerical simulations of the Earth’s interior. The spiral grid presented in this paper offers striking advantages compared to the commonly used grids based on projected triangulated platonic solids such as the cube, rhomboid or icosahedron (Ronchi 96, Baumgardner 85). Unique features of the spiral grid are the complete removal of symmetries with a freely selectable lateral and radial resolution and the ability to refine certain areas of interest, as well as the option of having a very small inner radius to outer radius ratio. Nonetheless, all beneficial geometrical properties of the Voronoi cells remain present.

It is possible to distribute grid points almost uniformly and therefore achieve an approximately constant volume of grid cells, as presented in section 2.

The geometrical properties of a Voronoi grid favor a finite-volume discretization of the required equations and in combination with the spiral grid provide among the previously discussed properties a single array alignment for one shell along the spiral path. This housekeeping method makes it easy to identify adjacent cells. Varying depth-dependent resolutions gives the user the choice to refine certain areas of interest, as well as the chance to have a very small inner radius to outer radius ratio.

The Thomson domain decomposition as described in section 2.6 makes the spiral grid ready for massive parallel computing. Through a minimization of ghost-cells, the overhead due to data exchanges becomes minimal as well. The number of domains is freely selectable and not restricted to geometrical properties. Various efficiency tests were conducted on different computing architectures, with a peak performance speedup of 200.73 for 256 CPUs.

A detailed statistical analysis in section 3 shows the advantages of a centroidal shift towards a CVD. Our method decreases the amount of neighbors while maintaining the Voronoi properties of the grid. The centroidal shift has a positive influence on the final coefficient matrix structure and therefore reduces computational resources.

In section 4, the spiral grid is tested against heat diffusion through a spherical shell with fixed boundary conditions by comparing numerical and analytical solutions. The spiral grid is combined with a finite volume code for mantle convection to simulate thermal convection in a spherical shell. The convection code, which is based on the centroidal Voronoi diagram, successfully reproduces previously published results of steady-state convection with a tetrahedral and a cubic flow pattern [Stemmer et al., 2006]. Nusselt-numbers and rms-velocities agree within a few percent with the published values. Because of the flexibility of the spiral-Voronoi grid approach, this mantle convection model lays a promising groundwork for further development of more complex mantle convection models, such as those including spatial varying fluid parameters like temperature dependent viscosity.

*Acknowledgements.* The authors would like to thank D. Breuer and T. Spohn of the German Aerospace Center (DLR) for providing the facilities utilized during this study. This work was carried out under the HPC-EUROPA project (RII3-CT-2003-506079), with the support of the European Community - Research Infrastructure Action of the FP6.

## References

- P. ALLIEZ, E. COLIN DE VERDIERE, O. DEVILLERS and M. ISENBURG (2005), Centroidal Voronoi diagrams for isotropic surface remeshing, *Elsevier Graphical Models*, 67, 204-231.
- S. BALAY, K. BUSCHELMAN, V. ELJKHOUT, W. D. GROPP, D. KAUSHIK, M. G. KNEPLEY, L. CURFMAN MCINNES, B. F. SMITH and H. ZHANG (2004), *PETSc Users Manual*, ANL-95/11 - Revision 2.1.5, Argonne National Laboratory.



- C. B. BARBER, B. P. DOBKIN and H. T. HUHDANPAA (1996), The Quickhull algorithm for convex hulls, *ACM Trans. on Mathematical Software*, 22(4), 469-483.
- J. R. BAUMGARDNER and P. O. FREDERICKSON (1985), Icosahedral discretization of the spherical shell, *SIAM J. Numerical Analysis*, 22, No. 6.
- D. BERCOVICI, G. SCHUBERT and G. A. GLATZMAIER (1989), Three-dimensional spherical models of convection in the Earth's mantle, *Science*, 244, 950-955.
- F. H. BUSSE (1975), Patterns of convection in spherical shells: Part 2, *J. Fluid Mech.*, 72, 67-85.
- B. C. CARLSON and E. M. NOTIS (1981), Algorithms for incomplete elliptic integrals, *ACM Transactions on Mathematical Software*.
- G. CHOBLET (2005), Modelling thermal convection with large viscosity gradients in one block of the 'cubed sphere', *Journal of Computational Physics*, 205, 269-291.
- G. DU, V. FABER and M. GUNZBURGER (1999), Centroidal Voronoi tessellations: Applications and algorithms, *SIAM Review*, 41, 637-676.
- Q. DU and M. GUNZBURGER (2002), Grid generation and optimization based on centroidal Voronoi tessellations, *Applied Mathematics and Computation*, 133, 591-607.
- J. H. FERZIGER and M. PÉRIC (2002), *Computational Methods for Fluid Dynamics*, 3rd ed., 423 pp., Springer-Verlag New York.
- C. A. J. FLETCHER (1991), *Computational Techniques for Fluid Dynamics*, Vol. 2, 2<sup>nd</sup> ed., Springer, Berlin.
- G. A. GLATZMAIER, (1988), Numerical simulations of mantle convection: Time-dependent, three-dimensional, compressible, spherical shell, *Geophys. Astro. Fluid*, 43, 223-264.
- H. HARDER (1998), Phase transitions and the three-dimensional planform of thermal convection in the Martian mantle, *J. Geophys. Res.*, 103, 16775-16797.
- Y. IWASE (1996), Three-dimensional infinite Prandtl-number convection in a spherical shell with temperature-dependent viscosity, *J. Geomag. Geoelectr.*, 48, 1499-1514.
- W. P. JONES and K. R. MENZIES (2000), Analysis of the Cell-Centered Finite Volume Method for the Diffusion Equation, *Journal of Computational Physics*, 165, 45-68.
- L. JU, Q. DU and M. GUNZBURGER (2002), Probabilistic methods for centroidal Voronoi tessellations and their parallel implementations, *Elsevier Parallel Computing*, 28, 1477-1500.
- A. KAGEYAMA, T. SATO, K. WATANABE, R. HORIUCHI, T. HAYASHI, Y. TODO, T. WATANABE and H. TAKAMARU (1995), Computer simulation of a magnetohydrodynamic dynamo, II, *Phys. Plasmas*, 2, 1421-1431.
- S. I. KARATO and P. WU (1993), Rheology of the upper mantle: A synthesis, *Science*, 260, 771-778.
- S. LLOYD (1982), Least Square quantization in PCM, *IEEE Trans. Infor. Theory*, 28, 129-137.
- J. MAC QUEEN (1967), Some methods for classification and analysis of multivariate observations, in: L. Le Cam, J. Neyman (Eds.), *Proceedings of the Fifth Berkeley Symposium on Mathematical Statistics and Probability*, Vol. I, University of California, 281-297.
- S. V. PATANKAR (1980), *Numerical Heat Transfer and Fluid Flow*, McGraw-Hill, New York
- J. T. RATCLIFF, G. SCHUBERT and A. ZEBIB (1996), Effects of temperature-dependent viscosity on thermal convection in a spherical shell, *Physica D*, 97, 242-252
- C. M. RHEE and W. L. CHOW (1983), A numerical study of the turbulent flow past an airfoil with trailing edge separation, *AIAA J.* 21, 1525-1532.
- C. R. RONCHI IACONO and P. S. PAOLUCCI (1996), The "Cubed Sphere": A New Method for the Solution of Partial Differential Equations in Spherical Geometry, *Journal of Computational Physics*, 124, 93-114.
- G. SCHUBERT (2001), *Mantle Convection in the Earth and Planets*, 940 pp., Cambridge Univ. Press, New York.
- K. STEMMER, H. HARDER and U. HANSEN (2006), A new method to simulate convection with strongly

- temperature- and pressure-dependent viscosity in a spherical shell: Applications to the Earth's mantle, *Phys. Earth Planet. In.*, 157, 223-249.
- D. SUNDAY (2002), Fast polygon area and Newell normal computation, *Journal of Graphics Tools*, 7(2), 9-13.
- M. TABATA and A. SUZUKI (2000), A stabilized finite element method for the Rayleigh-Bénard equations with infinite Prandtl number in a spherical shell, *Comput. Methods Appl. Mech. Eng.*, 190, 387-402.
- P. J. TACKLEY, D. J. STEVENSON, G. A. GLATZMAIER and G. SCHUBERT (1993), Effects of an endothermic phase transition at 670 km depth on a spherical model of convection in Earth's mantle, *Nature*, 361, 699-704.
- J. J. THOMSON (1904), On the Structure of the Atom: an Investigation of the Stability and Periods of Oscillation of a number of Corpuscles arranged at equal intervals around the Circumference of a Circle; with Application of the Results to the Theory of Atomic Structure, *Philosophical Magazine Series 6, Volume 7, Number 39*, pp. 237-265.
- M. YOSHIDA and A. KAGEYAMA (2004), Application of the Yin-Yang grid to a thermal convection of a Boussinesq fluid with infinite Prandtl number in a three-dimensional spherical shell, *Geophys. Res. Lett.*, 31, L12609.
- D. J. WALES and S. ULKER (2006), Structure and Dynamics of Spherical Crystals Characterised for the Thomson Problem, *Phys. Rev. B*, 74, 212101.
- J. WEERTMAN (1970), The creep strength of the Earth's mantle, *Rev. Geophys.*, 8, 45-168.
- S. ZHONG, M. T. ZUBER, L. MORESI and M. GURNIS (2000), Role of temperature-dependent viscosity and surface plates in spherical shell models of mantle convection, *J. Geophys. Res.*, 105, 11063-11082.